Nanotechnology

Semiconductor nanowire arrays for optical sensing: a numerical insight on the impact of array periodicity and density

To cite this article before publication: Luca Zagaglia *et al* 2021 *Nanotechnology* in press https://doi.org/10.1088/1361-6528/abff8b

IOP Publishing Journal Title
Journal **XX** (XXXX) XXXXXX https://doi.org/XXXX/XXXX

Semiconductor nanowire arrays for optical sensing: a numerical insight on the impact of array periodicity and density

Luca Zagaglia[1], Valeria Demontis[2], Francesco Rossella[2] and Francesco Floris[1]

[1] Tyndall National Institute, University College Cork, Cork, Ireland
[2] NEST Laboratory, Scuola Normale Superiore and Istituto Nanoscienze-CNR, Pisa , Italy

E-mail: luca.zagaglia@tyndall.ie and francesco.floris@tyndall.ie

Received xxxxxx
Accepted for publication xxxxxx
Published xxxxxx

Abstract

Recent advances in the nanofabrication and modelling of metasurfaces have shown the potential of these systems in providing unprecedented control over light-matter interactions at the nanoscale, enabling immediate and tangible improvement of features and specifications of photonic devices that are becoming always more crucial in enhancing everyday life quality. In this work, we theoretically demonstrate that metasurfaces made of periodic and non-periodic deterministic assemblies of vertically aligned semiconductor nanowires can be engineered to display a tailored effective optical response and provide a suitable route to realize advanced systems with controlled photonic properties particularly interesting for sensing applications. The metasurfaces investigated in this paper correspond to nanowire arrays that can be experimentally realized exploiting nanolithography and bottom-up nanowire growth methods: the combination of these techniques allow to finely control the position and the physical properties of each individual nanowire in complex arrays. By resorting to numerical simulations, we address the near- and far-field behavior of a nanowire ensemble and we show that the controlled design and arrangement of the nanowires on the substrate may introduce unprecedented oscillations of light reflectance, yielding a metasurface which displays an electromagnetic behavior with great potential for sensing. Finite-difference time-domain numerical simulations are carried out to tailor the nanostructure parameters and systematically engineer the optical response in the VIS-NIR spectral range. By exploiting our computational-methods we set-up a complete procedure to design and test metasurfaces able to behave as functional sensors. These results are especially encouraging in the perspective of developing arrays of epitaxially grown semiconductor nanowires, where the suggested design can be easily implemented during the nanostructure growth, opening the way to fully engineered nanowire-based optical metamaterials.

Keywords: metamaterials, metasurfaces, semiconductor nanowires, core-shell, optical reflectance, sensing, numerical simulations

1. Introduction

The control of light propagation is a central challenge in several areas of physics, as it is at the core of all the systems and technologies which use photons as signal carriers.

Photonics [1,2], information and communication technologies [3], quantum technologies [4,5], sensing [6,7] and machine learning [8] are just a few fields where the accurate control of light propagation and properties are amongst the key research aspects. Metamaterials have emerged in this context as powerful systems for light manipulation at spatial scales typically much smaller than the wavelength [9,10]. These are artificial media composed of arrays of resonant subwavelength structures, which can be designed in order to obtain effective medium properties which go beyond those of natural materials, unleashing the potential for an unprecedented control of light-matter interactions at the nanoscale [11,12]. All-dielectric metamaterials, in particular, are desirable at optical frequencies as they are largely free of Ohmic losses and can be realized exploiting nanostructures with geometrical dimensions comparable to the diffraction limit resolution, resulting in an easy integration into tiny volumes [13,14,15]. Metasurfaces, a subset of metamaterials with reduced dimensionality, captured the interest of the scientific community as they offer stunning opportunities for advanced optical manipulation in many cutting-edge photonic applications [16,17,18]. Metasurfaces in fact circumvent the limitations of conventional optical components and open unexplored routes to entirely new functionalities to engineer many light properties, including amplitude [18], phase [18], polarization [17,19], angular momentum [20], etc. Moreover, with respect to 3D metamaterials, metasurfaces benefit from simplified fabrication processes and easier integration with on-chip photonic devices owing to their planar nature [21].

In this framework, artificial calibrated arrangements of vertically aligned dielectric quasi one-dimensional structures, shaped as nanowires (NWs), provide ideal platforms to control photonic bandgap materials [13-22], and more in general are of considerable importance for building-blocks promising for next-generation sensing devices [23]. Indeed, arrays of vertically aligned one-dimensional NWs have demonstrated great potential in photonic applications due to their ability to tightly confine optical signals and to the possibility to easily adjust the growth parameters in order to tune the assemblies' optical properties during the growth [24]. Moreover, the growth mechanisms of these nanostructures allow the realization of light emitting nanodevices, such as single photon emitters [25] and lasers [26], which can be easily realized in the individual NWs during the growth. Thanks to the progress in nanofabrication and growth techniques, it is nowadays possible to engineer nanowire arrays by precisely controlling the nanowires physical properties and their accurate location over the grow substrate [27], opening the way to the realization of systems with finely tailored optical response. Optimized ordered arrays of semiconductor nanowires with exceptional absorption properties [28,29] and light management capabilities [30] have been demonstrated in recent years. Moreover, ordered arrays of heterostructured nanowires implementing functional devices in each individual nanowire, such as photovoltaic devices [31,32], lasers [33], and photodetectors [34] were also reported. In this context, computational methods are vital to guide the design of nanowire array configurations, by properly and simultaneously optimizing the single NW features (e.g. geometrical features and aspect ratio) as well as the assembly parameters (e.g. the NW density and arrangement on the substrate). This allows to engineer non-trivial electromagnetic responses tailored for specific applications. As a consequence, a complete design procedure calibrated on the application requirements can be envisioned, providing a very effective design tool, preliminary to the experimental realization and characterization of the metasurface. Applications of computational methods for supporting the design of nanowire arrays for specific applications such as photovoltaics have been reported previously [35-36].

In this work, we propose an extended computational study regarding the light scattering properties of assemblies of vertically aligned NWs disposed either in crystalline (ordered) and quasicrystalline (disordered) arrays. Varying the geometrical parameters either of the single NW and the array, we show how optical modulations can be introduced and tuned on purpose in the reflectance (*R*) spectrum in the VIS-NIR spectral range. A proper parameter space, selected in accordance with the features that are accessible resorting to the available fabrication techniques, is chosen to obtain metasurfaces able to selectively enhance specific resonances in *R*, engineered for bio-sensing applications. Campaigns of three-dimensional Finite-Different-Time-Domain (3D-FDTD) simulations are exploited to resolve the light scattering process behind the crystal/quasicrystal-light interaction. Furthermore, 3D-FDTD simulations are used to mimic sensing measurements to highlight the sensitivity in capturing variations in the background refractive index, and the results are supported by electromagnetic field expansion for a deeper comprehension.

In summary, the rationale behind our work consists in undergoing a theoretical study of the optical response in far field (reflectance) of semiconductor nanowire arrays, motivated by potential applications in sensing and supported by the possibility to effectively realize the proposed material platforms - the systems under study are in fact physically realizable with the state of the art of nanotechnology. The motivation of our work is manifold:

i. exploring the possibility of tuning the reflectance spectra by varying the geometrical features of NW metasurfaces in order to observe optical oscillations in the desired wavelength range;

ii. investigating the sensitivity capabilities of the selected metasurfaces, performing a calculation of the relative reflectance variation;

iii. demonstrating that the engineered features of the electromagnetic field are compatible with sensing measurements, by performing an electromagnetic field expansion analysis.

Focusing on the definition of a computational design protocol, we provide a step-by-step method to engineer the optical response taking into account the experimental constrains of state-of-the-art growth techniques. As a matter of fact, with this work we are establishing a roadmap to analyze the sensing capabilities of fully engineered all-dielectric nanowire metasurfaces, a subfield in nanoscale photonic research that is attracting the interest of the scientific community.

2. Materials and Methods

The metasurfaces were modelled as GaAs bulk substrates overlaid with assemblies of vertically aligned NWs acting as discrete scatterers. Three different NW systems were studied: homogenous (H) NWs, made of GaAs only, core-shell (CS) and tapered core-shell (T-CS) NWs, consisting in cylindrical radial heterostructures, where the core and the shell are made of GaAs and $Al_xGa_{1-x}As$ (with x=0.1), respectively. The latter geometries were selected as the optical responses of analogues metasurfaces have already been investigated and successfully exploited for similar purposes [37].

The NW geometrical parameters, reported in Figure 1 panel (a) with the corresponding numerical values summarized in Table 1 in the nanowire models table, were chosen in accordance with realistic feature ranges for NW arrays grown by bottom-up techniques. Two assemblies' categories were considered taking into account the periodic and non-periodic feature of the crystal and quasicrystal displacement: the crystal ones are square or triangular arrays characterized by two different degree of symmetries, whereas the quasicrystal array was built mimicking the Fermat's spiral pattern, as reported in Figure 1 panel (b) with the corresponding numerical values summarized in Table 1 in the array model table. The NW density derives from both the NW geometrical dimensions and the surface patterning features, so that 5 and 10 $NWs \cdot \mu m^{-2}$ were taken into account.

2.1 Identifying a realistic parameter space: a bird's eye view on fabrication techniques and features

The metasurfaces investigated in this paper correspond to structures that can be experimentally manufactured and are made of ordered arrays of dielectric NWs. The investigated parameter space was then selected according to the experimentally accessible ranges of variation for the metasurface features. In this section we briefly review the main fabrication techniques of metasurfaces made of ordered arrays of semiconductor nanowires.

The fabrication of these nanostructures benefits from the advances in nanofabrication and growth techniques which allows to design engineered NW patterns with a very fine control over the size, shape, material composition, location and orientation of each individual NW. Ordered arrays of NWs can be fabricated by several methods, which can be categorized into two paradigms: top-down or bottom-up approaches [38]. Top-down fabrication is a subtractive technique, which consists in carving the NWs from the bulk materials, according to a lithographically defined pattern, by means of anisotropic etching (dry or wet etching). This technique is mature and scalable and it allows NW patterning with high reproducibility and accurate size control. However, this technique requires a fine control over the etching process, which is a challenging task. Moreover, a significant process complexity is introduced when the lattice mismatch between the NWs' materials and the substrate is substantial [39,40]. Top-down approaches also pose some restraints regarding the NW structures, materials and properties, by preventing the access to some material properties, which may not be accessible in the bulk form [38].

The bottom-up approaches are the most widely used techniques for the realization of ordered arrays of semiconductor NWs. They consist in self-assembly processes which mainly rely on two prominent techniques: vapor phase growth (vapor-liquid-solid or VLS method), which is at present the most commonly used technique for NW growth [41], and selective area epitaxy. Both the techniques enable the realization of engineered NW arrays, by exploiting lithographically prepatterned substrates, which are employed as templates to control the NW location and size.

VLS [42] is a metal catalyzed process, which exploits the reaction between a metal catalyst, in the form of a metal nanoparticle, and the semiconductors precursor gases to give rise to NW growth. By using this approach, the NWs composing an array can be individually seeded in a controlled fashion, in order to obtain highly ordered patterns. In fact, the metal nanoparticle size, shape and location, together with optimized growth parameters, determine the NW diameters, lengths, location, shape, crystal structure and other properties [43,44,45].

Selective area epitaxy, which includes catalyst-free and self-catalyzed growth, rely on the use of dielectric mask templates to grow position controlled NWs without the aid of metal droplets [46, 47]. In this case, an array of holes in a dielectric thin film act as nucleation point for the growth of NWs at determined locations. Also in selective area epitaxy, the NW size, location and properties can be tuned by properly optimizing the hole pattern in the oxide template

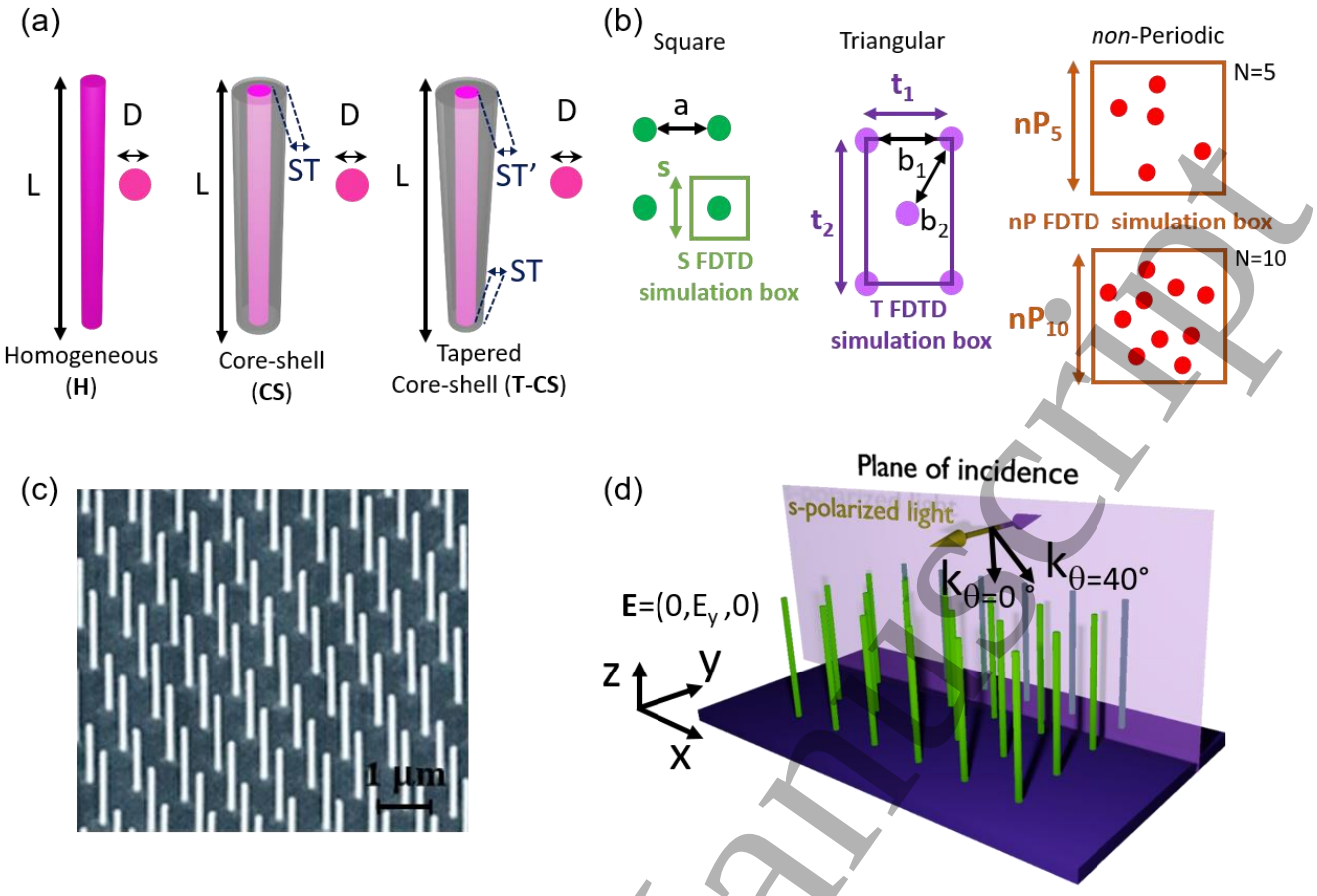

Figure 1: (a) A schematic representation of the three nanowire morphologies, and (b) a schematic representation of the three array models, together with an indication of the relevant parameters with their numerical values reported in Table 1. (c) Scanning electron micrograph of a bottom-up grown nanowire square array (reprinted with permission of Ref [52]). (d) Pictorial view of the ideal set-up and coordinate system for measuring the reflectance *R* simulated in this work, with S-polarized incident beam and two considered incident angles (θ=0° and θ=40°); the **k** wavevector along the x and z directions on the plane of incidence for the two incidence angles are shown.

Nanowire models	**D (nm)**	**L (nm)**	**ST (nm)**
Homogeneous (H)	50, 100, 150	750, 1000, 1250, 1500	- - -
Core-Shell (CS)	100	750, 1000, 1250, 1500	15, 30, 45
Tapered Core-Shell (T-CS)	100	750, 1000, 1250, 1500	ST (at base): 15, 30,45 ST' (at tip): ST+30

Array models	**N=5**	**N=10**
Square (S)	a=s=447nm	a=s=315nm
Triangular (T)	$b_1=t_1$=400nm b_2=540nm t_2=1000nm	$b_1=t_1$=400nm b_2=320nm t_2=500nm
non-Periodic (nP)	nP_5=1000nm	nP_{10}=1000nm

Table 1: "***Nanowire models***" table: for the three nanowire models considered in the work (homogeneous nanowires (H), core-shell nanowire (CS) and tapered core-shell nanowires (T-CS), the investigated values of the main geometrical nanowire parameters are reported (i.e. nanowire diameter (D), corresponding to the nanowire core diameter in the core-shell cases, shell thickness (ST) and, for the tapered case (T-CS), shell thickness at the nanowire's tip (ST'), ST being in this case the shell thickness at the base). **"*Array models*"** table: for the two explored nanowire densities (N=5 nanowire per μm^{-2} and N=10 nanowire per μm^{-2}) and for the three considered arrays (S-square, T-triangular and nP-non-Periodic), absolute values of the primitive vectors of the periodic arrays (a, b_1, b_2) and sizes of the FDTD cells (s, t_1, t_2, nP_5, nP_{10}) used for calculations.

and the growth parameters [48]. In both these methods, electron beam lithography and nanoimprint lithography are the most used techniques for the pattern definition, as they ensure the best precision for the realization of the seed array [43,44,49].

Bottom-up fabrication approaches are nowadays well established techniques to realize very high crystal quality NWs, with almost defect-free structures, even in the case of high lattice mismatching between the NW material and the substrate [41,50], as it is the case for III-V semiconductor NWs integrated on silicon platforms. Moreover, these techniques have also been demonstrated to be very suitable to realize sophisticated NW semiconductor heterostructures with atomically sharp interfaces. Bottom-up growth, in fact, allows a fine control on the chemical composition along the NW axis and in the radial direction, allowing to tailor the NW composition in different directions by changing the growth conditions during synthesis. NW solar cells [51], hard wall quantum dots [52,53,54] and core-shell [55,56] with atomically sharp interfaces have been realized. Moreover, the control of the growth parameters allows to obtain a straight control over the individual NW geometry. Figure 1 panel (c) shows a scanning electron micrograph of a bottom-up grown nanowire square array. A geometric NW feature which was confirmed as a relevant parameter to affect NW arrays optical properties [37,57,58], is tapering, which is one of the parameters considered in the present paper. Tapering is the systematic variation of the NW diameter along the axis, which results in NW with inclined sidewalls (both positive and negative). Tapering can be controlled during the growth by controlling some interacting growth parameters, namely the droplet contact angle and volume, the temperature and the precursors gas flows [40,59].

2.2 Computational Methods

FDTD numerical simulations of the optical specular reflectance spectrum (*R*) and the related electric field distributions were performed using Lumerical FDTD Solutions software [60]. We used the software built-in material database to define the optical parameters of both GaAs and AlGaAs.

The square (S) and triangular (T) FDTD arrays were built resorting to a customize external script where the only primitive vectors of the array base were specified, i.e. **a** for the S array and $\mathbf{b}_1$, $\mathbf{b}_2$ for the T array as reported in figure 1 panel (b); while the non-periodic (nP) ensemble was generated through a custom script to display the NWs positions following a polar coordinate representation (r,θ) of the Fermat's spiral given by $r = c\sqrt{n}$ and $\theta = n\varphi$, where r is the distance from the center, q is the angle, n is the NW index, c is the scaling factor, and φ is the golden angle. In our code, we used Bloch boundary conditions to calculate the response of the entire NWs assembly by simulating an opportune simulation box specific for each array models, as in figure 1 panel (b). In addition, the NW density was controlled selecting the geometrical dimensions for each simulation box, as reported in the array models table of table 1. A plane-wave source, which mimics a realistic light beam used for reflectance measurements, was used to inject the light into the simulation box in order to calculate the specular reflectance spectra with a background refractive index $n_{bg}=n_{air}=1$. The polarization state was chosen to be S as the oscillation direction of the electric field is perpendicular to the plane of incidence and thus independent of the propagation direction, as depicted in figure 1 panel (d). Two values related to the angle of incidence θ of 0° and 40° were considered in order to obtain two different projections of the **k** wavevector along the x and z directions on the plane of incidence.

A customized mesh with a resolution of 5nm was selected exploiting a mesh override around the NW region after performing appropriate convergence tests: not only the step size was reduced down to 3nm, but also a different sampling strategy was exploited using an auto-non uniform mesh of level 6.

An averaged time of roughly one hour for the square and triangular array and approximately five hours for the non-periodic nanowire assembly is needed to complete the simulation on a computer with a liquid-cooled 16-core processor (32 threads) and 64 GB of RAM. A campaign of about 900 simulations were run resulting in slightly more than two thousand machine time hours.

3. Results and Discussion

We apply our computational approach to identify realistic arrays of semiconductor NWs capable of unprecedented sensing performance in the VIS-NIR spectral range. The starting point is the selection of a substrate that exhibits a flat response in reflection across the (400÷1200) nm interval, compatible with the targeted application spectral range. Thus, the first step is the suppression of the substrate *R* spectrum in the targeted spectral range ensuring an initial condition exploitable for the introduction of localized optical oscillations. From the metastructure perspective, this can be obtained using a GaAs substrate and growing on top of it vertically aligned assemblies of H-NWs, in order to create a metasurface that displays the required optical-features, as similarly done in [61]. Then, to gain control on these optical modes and made them suitable for feasible measurements, it is necessary to introduce a resonator aiming at selecting specific wavelengths in the reflectance spectrum. This can be done by resorting to Fabry-Perot oscillations and consequently implementing a strategy to enhance their amplitude. This has been already proofed in [37], thus a core-shell NW made of a GaAs core surrounded by an AlGaAs

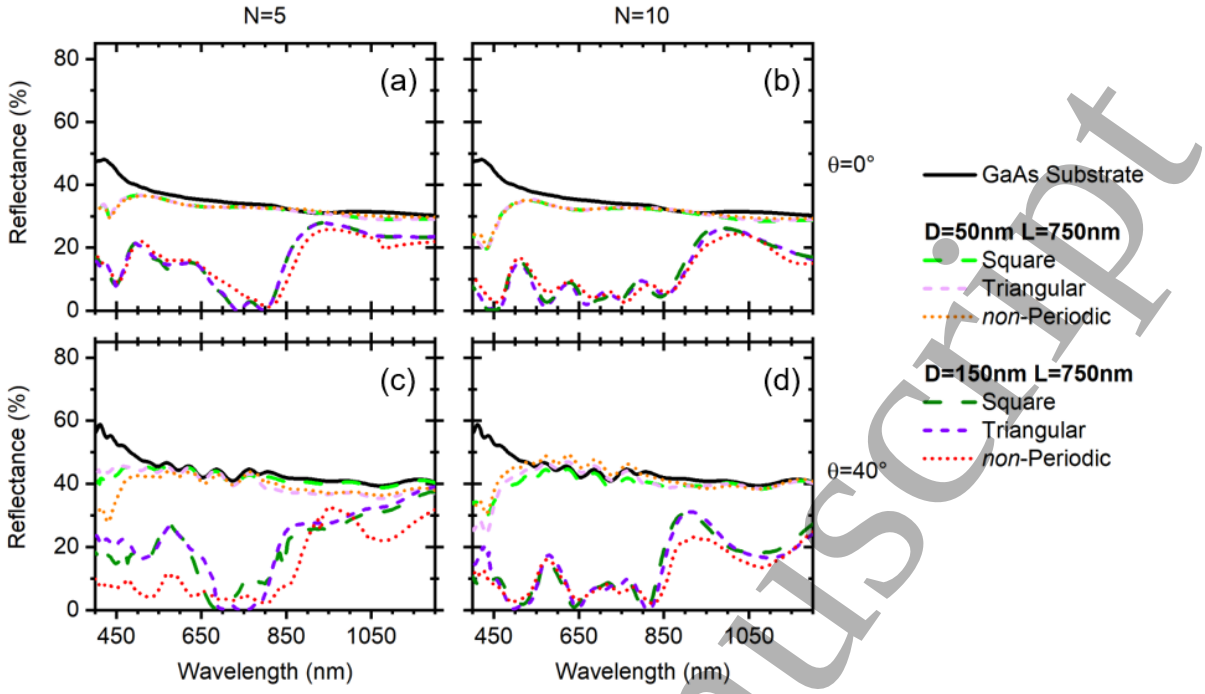

Figure 2: Selected reflectance spectra (*R*) calculated for different metasurfaces made of homogeneous nanowires having all the same height equal to 750nm: R spectra for a metasurface with a density of (a) 5 nanowires per μm^{-2} and (b) 10 nanowires per μm^{-2}, and for incidence angle of θ=0°; (c) *R* spectra for a metasurface with a density of 5 nanowires per μm^{-2} and (d) 10 nanowires per μm^{-2}, and for incidence angle of θ=40°. Each panel displays 7 curves: a black curve for the bare GaAs substrate, three curves for nanowires with 50nm diameter (one curve for each array model: light green dashed line for the square array, light purple dashed line for the triangular array and orange dotted line for the non-periodic array) and three curves for nanowires with 150nm diameter (dark green dashed line for the square array, dark purple dashed line for the triangular array and red dotted line for the non-periodic array). The *R* curves for the 50nm nanowire metasurface are very similar amongst each other and to the bare substrate curve.

shell was chosen, with the proper tapering. However, a precise tuning of the optical oscillations is not trivial due to the lack of determinism in such structures. Starting from the previous findings, we were interested in overcoming such limitation by tuning the optical oscillations in the NIR spectral region between (700÷1200)nm, which is of particular interest for bio-sensing applications. Therefore, it became necessary to exploit simultaneously both the array and the single NW geometrical-features. The goal is to detect a variation in the background refractive index through a shift in the wavelength positions of the aforementioned oscillations by analyzing the *R* spectra for the engineered metasurfaces.

3.1 Setting-up the Nanowire Metasurface

The suppression of the substrate *R* spectrum in the desired wavelength range is achieved starting from the evaluation of the far-field optical response, i.e. the *R* spectrum, in the VIS-NIR for the bare GaAs substrate. As shown in Figure 2, the substrate *R* for either θ=0° and θ=40° displays an approximately flat behavior across the (400÷1200)nm interval, which represents the initial requirement. Two different values of θ are investigated in order to be able to modify the interaction cross-section between the plane wave and the structures by changing the effective lattice constant seen by the incoming light, and as expected the interaction is higher at incident angle θ=40°, with respect to θ=0°. The substrate optical response is then modified, yielding to a desired effective refractive index, exploiting arrays of vertically aligned H-NWs to create a new material, i.e. a metasurface. The *R* spectrum of such H-NW metasurfaces constitutes the benchmark used to tailor the optical oscillations. The *R* spectra for these metasurfaces for different values of NW diameters (D), and heights (L) (all the investigated values are reported in table 1) were calculated for the square (S), triangular (T), and non-periodic (nP) arrays for both the NW densities and incident angles under investigation, in order to detect the required geometrical features of the NWs able to achieve the suppression of the *R*. A total of 288 specular spectra were calculated and figure 2 shows the *R* for two significant types of H-NW with D values of 50nm and 150nm, respectively, and the same L of 750nm useful to understand how these structures operate. In details, the *R* spectra of the metasurfaces composed by H-NWs with D=50nm do not show any sign of *R* suppression for all the array models at θ=0° and qualitatively their optical responses maintain a flat

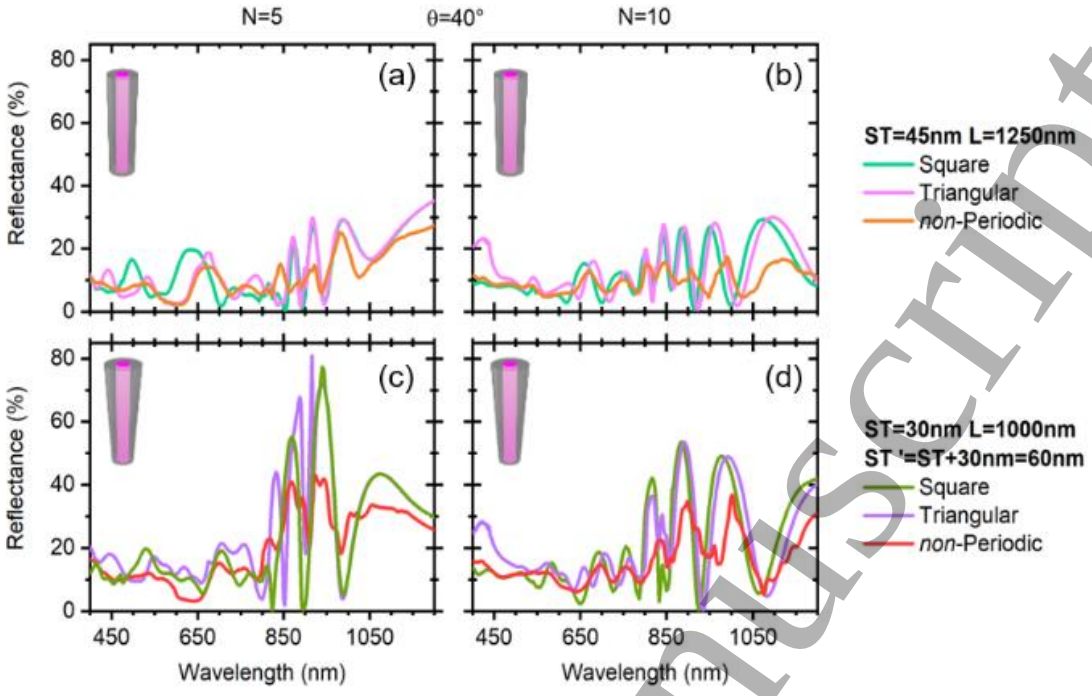

Figure 3: Selected reflectance spectra (R) calculated for fixed incidence angle of θ=40°, for metasurfaces made of: (a) and (b) core-shell (CS) nanowires with 50 nm diameter, 45 nm shell thickness (ST) and 1250nm height (L); (c) and (d) tapered core-shell (T-CS) nanowires with 50 nm diameter, 30 nm shell thickness at the base (ST), thus implying a shell thickness at the tip ST'=ST+30nm=60nm, and 1000nm height (L). (a) and (c) were calculated for a nanowire density of 5 nanowires per μm^{-2}, while (b) and (d) were calculated for a nanowire density of 10 nanowires per μm^{-2}. Each panel displays three curves, one for each investigated array model (light-green/green curve for the square array, pink/purple curve for the triangular array and orange/red curve for the non-periodic array).

trend across the wavelength range similar to the one of the GaAs substrate, as shown in panels (a) and (b), meaning that no significant variations of the refractive index are introduced due to the dimensions of the scatterers under the diffraction limit. Also at θ=40°, panels (c) and (d), the response maintains a similar trend, even though the interaction cross-section is higher. Only between the wavelength interval (400÷450)nm, where the dimensions of the scatterer become comparable to the effective wavelength, the *R* spectra show a tiny deep, sign of a variation in the refractive index introduced by the metasurface.

To overcome the diffraction limit, the suppression of *R* in specific intervals of the VIS-NIR is achieved thanks to a larger dimension of the scatterer, i.e. D=150nm. In particular, for the density of 5NWs•μm^{-2} a *R* suppression localized between (600÷900)nm is visible from figure 2, panels (a) and (c), while, for 10NWs•μm^{-2}, the *R* spectra are suppressed over a wider wavelength interval, i.e. (400÷1000)nm, panels (b) and (d). In addition, regardless of the angle, the overall *R* spectra shape remain similar fixed the NW density. In this case, the refractive index of the bare GaAs substrate is dramatically changed by the presence of NW assemblies modifying drastically the optical responses. Furthermore, because now the incoming plane wave interacts with the scatterer arrays, a significant difference between the *R* spectra for the two NW densities can be also appreciated. In fact, the optical response depends on the diffraction process between the incoming wave and the assemblies of NWs, thus it is also strongly dependent from the distances between the scatterers. For all these metasurfaces, a shoulder in the *R* spectra is present around 850nm; after, the optical response returns to display a flat trend, due to the diffraction limit. On the other hand, the spectral position of the left shoulder is controlled through the density of the NW arrays enabling to blue shift it over the left limit of the VIS-NIR interval for 10NWs•μm^{-2}.

Now, localized optical oscillations can be sustained in this region due to interference effects coming from either multiple scattering within the NWs and due to the all effective optical response of the metasurface that affects the far-field response. In particular, for 10NWs•μm^{-2}, multiple peaks with an amplitude between 10% and 20%, can be appreciated between (400÷1000)nm. Here, the exploitable interval is way wider than the averaged width of the oscillations enabling to resolve the peaks; while for 5NWs•μm^{-2}, the suppressed wavelength interval is too narrow and no optical oscillations can be appreciated.

3.2 Tuning the Nanowire Metasurface

The optical oscillations in the VIS-NIR interval are intentionally tuned by adding an AlGaAs shell to the H-NWs, creating a core-shell heterostructure, exploiting the refractive index contrast between the core-shell and shell-air interfaces acting as a resonator, i.e. Fabry-Perot cavity.

The optical oscillations derive from the selection performed by the Fabry-Perot cavities that store energies at specific wavelengths, which results in a lack of signal in the *R* spectrum, i.e. oscillation minima affecting consequently the far-field response. A series of 288 FDTD-simulations were performed to collect the *R* spectra for Core-Shell (CS) metasurfaces for all the array models and the incident angles, with a L, spanning from 750nm to 1500nm, a CS width values, called ST, varying between 15nm and 45nm and a D value of 100nm. This specific D was chosen taking into account the diffraction limit ensuring that, also for 10NWs•μm^{-2}, there was no overlap between the shells of adjacent CS-NWs. The values and a sketch of the CS-NW geometry is reported in figure 1. Figure 3 panel (a) and (b) show the *R* spectra for the S-, T-, and nP-arrays for both the densities and θ=40° with a ST value of 45nm and L=1250nm. The *R* spectrum of this particular metasurface was selected as the best overall results in terms of the optical oscillations for both the NW densities. As previously mentioned, the θ=40° incident angle allows for higher interaction cross-section between the plane wave and the CS-NWs, resulting in effective lattice constant compatible with optical oscillations in the desired (700÷1200)nm interval, exploitable for sensing applications. A total of three and five distinct major peaks arise between (800÷1200)nm for 5 and 10NWs•μm^{-2}, respectively, with the right shoulder shifted further than 1050nm, for the S-, and T-arrays. For these arrays, the available optical modes of the cavity interact coherently throughout the periodic structure enabling a constructive interference process supporting the optical oscillations. Equivalently, this can be seen in terms of a Bloch wave that propagates across the array enabling a coherent cross-talk between adjacent CS-NWs. On the contrary, the nP-arrays display a more "noisy" far-field response, with barely appreciable optical oscillations. This behavior is related to the lack of a periodicity in these structures, which generates a *R* spectrum dominated by a non-coherent interference process resulting in an averaged ensemble response dependent on the NW density. A greater number of optical oscillations can be seen at 10NWs•μm^{-2} density where, as shown in the previous section, a wider reflectance suppression region was demonstrated. Furthermore, it can be noticed that the same optical oscillations are present for all the array models as a consequence of the excitation of optical modes proper of the Fabry-Perot cavity of the scatterer; on the other hand, the wavelength shift of the peaks is a consequence of the scatterer disposition in the array affecting their cross-talk and consequently the constructive interference process. Finally, in the spectral region below 800nm, the *R* spectra show little optical modulations as the confinement process of the light derived from the mutual effect of the Fabry-Perot cavities of the single resonator and the interaction of these optical modes across the array is less efficient in this spectral region.

In order to make these optical oscillations suitable for sensing, their intensities can be increased enhancing the number of reflections that the light undergoes between the CS-NWs and the substrate, increasing the overall reflectivity of the scatterers. In this framework, an inverse tapering of the AlGaAs shell can be used to improve the confinement of the optical cavity modes in a tinier geometrical space. Again, a series of 288 simulations was performed for tapered core-shell (T-CS) NW metasurfaces, for all the array models and θ values, with D=100nm, L spanning from 750nm to 1500nm, a tapered shell with a bottom width, called ST, varying between 15nm and 45nm, and a higher top shell width, indicated as ST', equal to ST'=ST+30nm. This ensures a single tapering angle across the T-CS NW height. All the previous D, L, ST, and ST' values as well as a sketch of the T-CS NW are reported in figure 1. The D dimension was maintained equal to the CS-NW metasurface for the same aforementioned reason. Figure 3 panel (c) and (d) show the *R* spectra for the S-, T-, and nP-arrays for both the densities and θ=40° with a ST value of 30nm and L=1000nm.

The R spectra of these six specific metasurfaces display the strongest enhancement of the optical oscillations, i.e. the highest peak-to-valley ratio, amongst all other T-CS NW metasurfaces for either the 5 NWs•μm-2 and 10 NWs•μm-2, when illuminating the structures at θ =40°. Multiple main optical oscillations can be noticed for both densities for all the array models with an increased intensity of the oscillation up to roughly 80% for 5NWs•μm^{-2} and 50% for 10NWs•μm^{-2} in the spectral region (800÷1200)nm. Here, the simultaneous effect of constructive interference process established in the shells of each NW - the Fabry-Perot cavities - and the ones arising from the multiple reflection between the tapered-shell and the substrate improve the trapping of the light and, consequently, the selection of specific optical frequencies performed by the Fabry-Perot cavities. Thus, the specular *R* spectra of the metasurfaces display improved optical features resulting in more intense optical oscillations. Also in this case, the oscillations are related to the optical modes proper of the resonators, so the *R* modulations are equal for all the array models. In particular, the optical oscillations can be also seen for the nP-arrays, even though the non-coherent interference processes between the T-CS NWs affect their amplitudes with a less sharp and intense modulations.

Now, six different metasurfaces for either the 5NWs•μm^{-2} and 10NWs•μm^{-2} densities made resorting to T-CS NWs

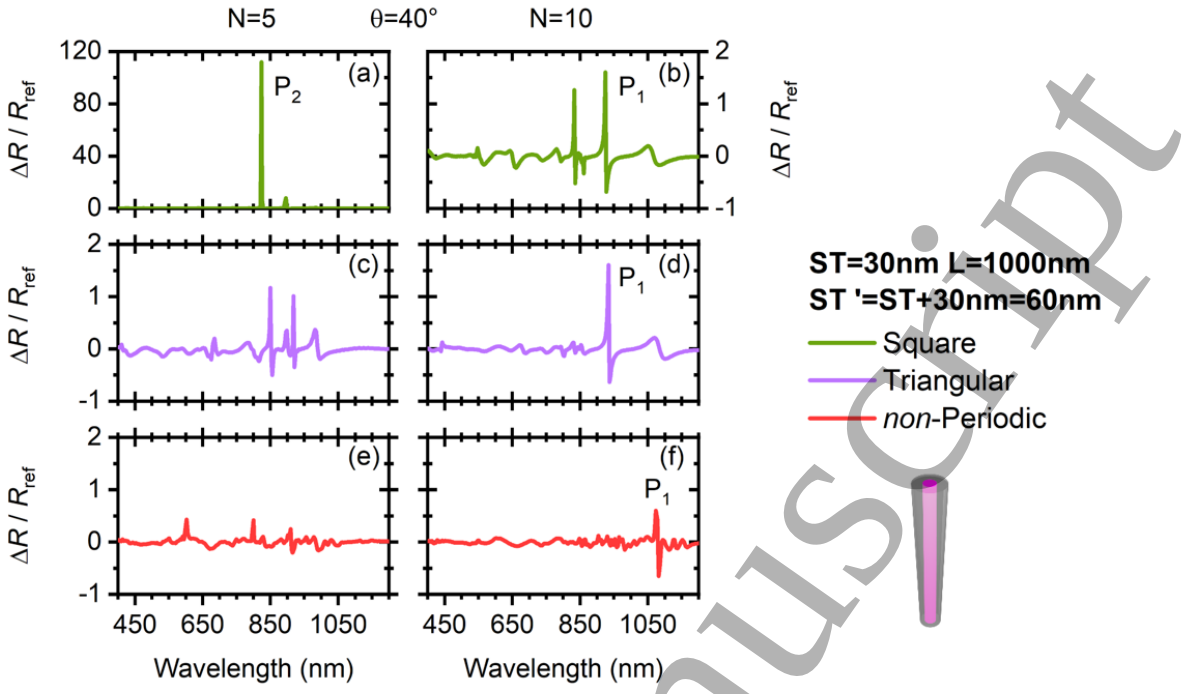

Figure 4: Relative reflectance variation ($\Delta R/R_{ref}$) induced by a 1% perturbation in the background refractive index, with respect to air, for: (a) and (b) square array, (c) and (d) triangular array, (e) and (f) non-periodic array of tapered core-shell (T-CS) nanowires. All the calculations were performed considering the same individual T-CS nanowire geometry (D=50nm, ST= 30nm, ST'=60 nm and length L=1000nm), a fixed incidence angle of θ=40° and: (a), (c) and (e) density of 5 nanowires per μm^{-2}; (b), (d) and (f) nanowire density of 10 nanowires per μm^{-2}.

with L=1000nm, and ST=30nm have been identified as potentially interesting for bio-sensing applications. In fact, these metasurfaces meet the sensing requirements of having a *R* spectrum in the VIS-NIR characterized by extended amplitudes of the optical oscillations, and sharp minima, with an intensity as closer as possible to 0%, at specific wavelengths. However, it is not straightforward to derive the sensing performances just exploiting the *R* spectra, but this needs a separate evaluation.

3.3 Sensing applications

The *R* spectra of figure 3 display optical oscillations tuned in air, i.e. background refractive index $n_{bg}=n_{air}=1.00$. In particular, the *R* spectrum is a function of the effective refractive index of the metasurface, which in turn depends also on the n_{bg}. A small perturbation of the n_{bg} can be exploited to change slightly the features of the *R* spectrum, such as the amplitudes of the optical oscillations avoiding a drastically change of the effective refractive index with a consequence detuning of the optical oscillations. These small variations in the *R* spectrum can be used for sensing applications, after specific tuning and proper functionalization depending on the application, with the aim of detecting, for instance, a temperature variation, or a change in the concentration of a targeted substance etc.

As no benchmark for these all-dielectric metasurfaces for sensing applications has been reported so far, a variation of 1% of the n_{bg}, from $n_{ref}= n_{bg}=n_{air}=1.00$ to $n_{bg}=n_p=1.01$, was found adequate to perturb the *R* spectrum without drastically modifying the effective refractive index of the metasurface to introduce a radically change of the metamaterial itself.

The ability in reacting to this external change can be studied exploiting the relative variation of the reflectance, also called dispersive signal in analogy with plasmonic sensing measurements of the relative reflectance [63],

$$\frac{\Delta R}{R_{\mathrm{ref}}(\mathrm{n_{ref}})} = \frac{R_{\mathrm{p}}(\mathrm{n_p}) - R_{\mathrm{ref}}(\mathrm{n_{ref}})}{R_{\mathrm{ref}}(\mathrm{n_{ref}})}$$

where R_{ref} is the reference *R* spectrum calculated in air, and R_p is the *R* spectrum calculated with a n_p value of 1.01.

Twelve FDTD simulations were run to evaluate the R_p spectra between (400÷1200)nm for the selected metasurfaces with an impinging angle θ of 40°, in accordance with the simulation results proposed in the previous section. Thus, taking advantage of the spectra reported in figure 3 panel (c) and (d) used as references, the relative variation of the reflectance was evaluated and the corresponding results are reported in Figure 4. Different spikes can be detected in figure 4 indicating where optical oscillations in the R_{ref} undergo a variation in R_p. If the variation affects a minimum,

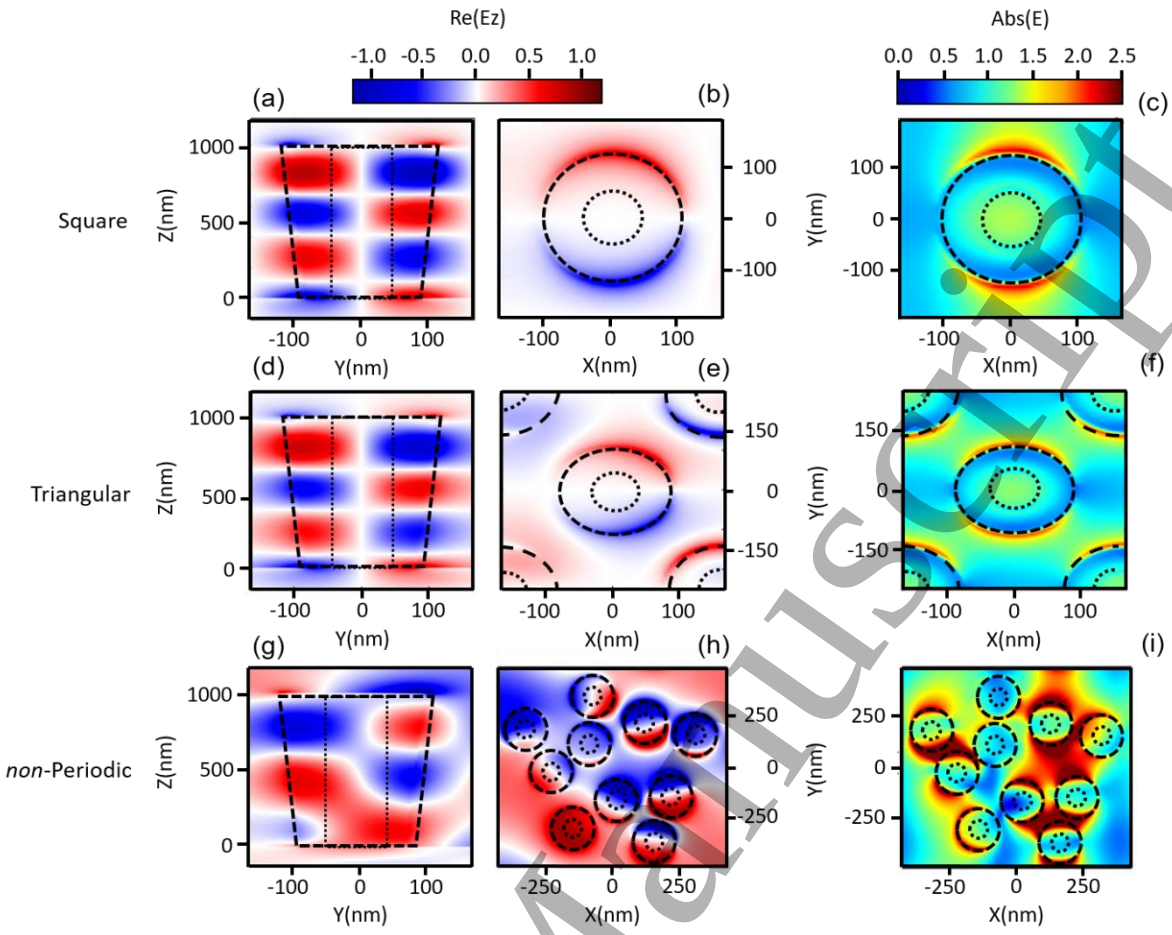

Figure 5: E_z component and absolute value of the electric field calculated in the region around one individual tapered core-shell nanowire, at incidence angle θ=40°, for metasurfaces with nanowire density of 10 nanowires per μm^{-2} and three different array models: square: (a), (b), (c); triangular: (d), (e), (f) and non-periodic: (g), (h), (i). For the three arrays, the simulation wavelengths correspond to the spike positions of P_1 in figure 4. (a), (d) and (g) transversal cross sections; (b), (e), (h) top-view of the E_z component evaluated at Z=1000nm; (c), (f) and (i) top-view of the absolute value of the electric field evaluated at Z=1000nm. The x, y, z directions are in accordance with reference system of figure 1 panel (d).

this spike might be associated to a spatially confined Fabry-Perot mode potentially suitable for sensing. Moreover, the electric field proper of this spatially confined Fabry-Perot mode needs to be mainly TM-polarized, i.e. along z direction. This condition guarantees a dipolar expansion shape for the electric field with an oscillation orientation that is orthogonal to the metasurface resulting in an in-plane emission giving a suppression of the reflectance.

Two spikes P_1 and P_2 were selected to analyze the corresponding electromagnetic expansion. P_1 was selected as the first peak moving from higher to lower wavelengths. The peak positions for the three different array models are close enough to suppose to be generated by an equivalent spatially confined Fabry-Perot mode. Thus, its electric field expansion is expected to be similar giving rise to a common response to a variation of the background refractive index resulting in a minimum in the reflectance spectra if TM-polarized. P_2 was chosen due to its high intensity, up to two order of magnitudes greater respect to P_1. Reasonably, the combination of the ability of the single NW in supporting the proper Fabry-Perot modes as well as an optimized spatial coherency due to the highest symmetry proper of the S-array is able to overcome the impact of the reduced interaction cross section proper of the lower NW density.

Four FDTD simulations were run to calculate the electromagnetic field for the aforementioned arrays at the wavelengths proper of P_1 and P_2 (three for 10NWs•μm^{-2} and one for 5NWs•μm^{-2}). Regarding 10NWs•μm^{-2}, the E_z scalar component, which is the main one related to the TM-polarized modes, is reported in panels (a), (b), (d), (e), (g), (h) of Figure 5 for all the different array models. It can be noticed that the light interacting with the metasurface can be scattered in plane thanks to the effect in rotating the polarization state of the impinging light given by the shell acting as a Fabry-Perot resonator. Thus, the entire metasurfaces can be described as coupled resonators resulting in an overall planar grating structure.

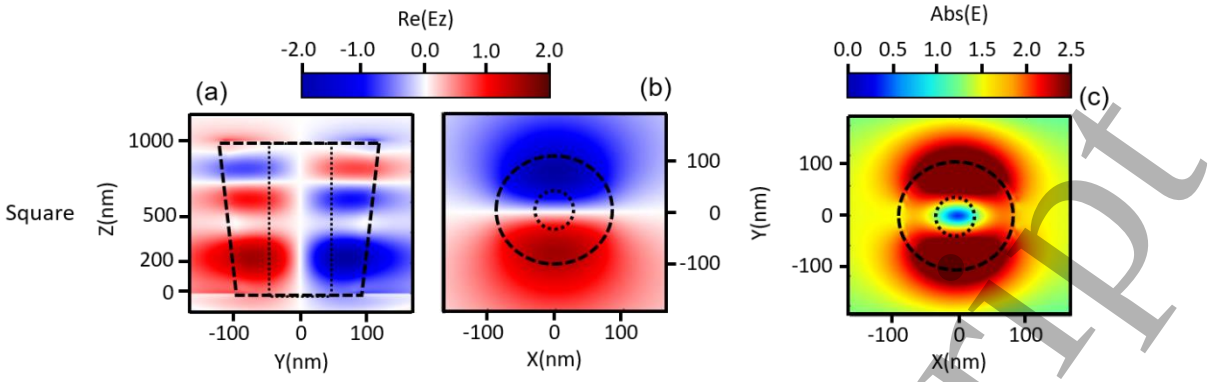

Figure 6: E_z component and absolute value of the electric field calculated in the region around one individual tapered core-shell (T-CS) nanowire, at incidence angle θ=40°, for a square nanowire array metasurface with nanowire density of 5 nanowires per μm^{-2} and wavelength corresponding to the spike position P_2 in figure 4: (a) transversal cross-section; (b) top view of the E_z component evaluated at Z=200nm; (c) top view of the absolute value of the electric field evaluated at Z=200nm. The x, y, z directions are in accordance with reference system of figure 1 panel (d).

Consequently, a portion of the energy carried by the incoming light is stored by the shell lacking in the reflectance spectrum. The mode expansion of the two periodic arrays show an ordered E_z spatial distribution inside the shell with a clear pattern for the maxima and minima. The field is well confined inside the shell with an exponential intensity decay in the background at the lateral interface. The overall features are essential requirements to achieve sensing capabilities for a metasurface. From panels (b) and (e), it can be noticed that the E_z expansion presents a ring shape typical of a dipolar mode. Panel (c) and (f) show the absolute value of the electric field and they can be used to understand the spatial distribution of the energy density. The latter display a pattern in accordance with the coherent cross-talk along the y direction for the S-array and along the diagonal directions for the T-array with the energy spread in the background. This is another requirement essential from the sensing prospective because is necessary to have as much electric field as possible in the active sensing region.

A different situation is found for the nP-array, as displayed in panels (g), (h), and (i). The E_z spatial distribution inside the NW is not symmetric anymore, panel (g), as no coherent cross-talk can be established between adjacent NWs reducing drastically the excitation of the Fabry-Perot modes, panel (h). No homogeneous electric field and energy density spatial distributions can be detected resulting in a non-coherent in-plane distribution. Nevertheless, the density energy is distributed mainly in the background satisfying the essential requirement related to the spread of the electric field giving anyway the chance to react to a background refractive index variation also for this non-periodic array.

Figure 6 shows the electromagnetic field expansion related to the spike P_2 displayed by the S-array for 5 NWs•μm^{-2}. The maxima and minima of the Fabry-Perot modes do not have the same intensity across the shell, as shown in panel (a), displaying an enhancement responsible for the huge P_2 spike in panel (a) of figure 4 and the wide oscillation in the reflectance spectrum in panel (c) of figure 3. Now, the energy density distribution displays a pattern in accordance with a coherent cross-talk with components along both the x and y directions. Eventually, this specific combination of features allows for a better sensitivity in detecting variation of the background refractive index resulting in the most promising metasurface for sensing, amongst all those considered.

4. Conclusions

Resorting to a systematic exploitation of 3D-FDTD simulations, in this work we have identified and theoretically investigated optical metasurfaces based on all-dielectric tapered core-shell nanowires NWs, made of a GaAs core and a AlGaAs shell, for bio-sensing applications. The reflectance spectra of these metasurfaces were engineered in the VIS-NIR step-by-step introducing and enhancing specific Fabry-Perot oscillations resorting to a tapered outer shell of the NWs with intensities up to 80%. Exploiting these optical oscillation, the relative variation of the reflectance was evaluated for different metasurfaces perturbing the corresponding *R* spectra introducing a variation of 1% in the background refractive index. The appearance of multiple spikes at specific wavelengths was demonstrated, mimicking the response of a functional sensor. Two spikes, i.e. P_1 and P_2, were selected to perform an electromagnetic field expansion demonstrating their association with a spatially confined Fabry-Perot mode suitable for sensing. The electromagnetic field expansion confirmed, for all the 10NWs•μm-2 array models, the equal origin of P_1 from the same spatially confined Fabry-Perot mode, which displayed a TM-polarization with E_z as the main scalar component of the electric field with a dipolar expansion shape. The E_z spatial distribution of the periodic arrays was found ordered, with a clear pattern of the maxima and minima, as well as a

coherent cross-talk sustained between adjacent NWs; on the contrary, the non-periodic array lacked of the previous features resulting in a less intense P1 spike respect to the one of the periodic arrays. In all the array models, the energy density showed a spatial distribution spread mainly in the background, essential requirement to react to a background refractive index variation. The same features of E_z were found for spatially confined Fabry-Perot mode of the spike P_2, observed for the 10NWs•μm-2 periodic arrays. Additionally, a peculiar enhancement of the intensity of the maxima and minima at the bottom of the NW, responsible for both the huge P_2 spike and the wide oscillations in the reflectance spectrum, was detected, resulting in being the most promising metasurface amongst those investigated. We believe that these results offer an insight regarding the physical mechanisms involved in the light propagation in this type of metasurfaces as well as detailed guidance on the effective tuning of the optical properties, therefore opening new perspectives in their potential for sensing applications.

Acknowledgements

This work was supported by Scientific Foundation Ireland (SFI), Grant NO. SFI-12/RC/2276_P2 (Ireland).

References

[1] Sun C et al. 2015 *Nature* **528** 534–538
[2] Guo X, Ding Y, Chen X, Duan Y and Ni X 2020 *Science* Advances **6** (29) 4142
[3] Yang Y, Yamagami Y, Yu X, Pitchappa P, Webber J, Zhang B, Fujita M, Nagatsuma T and Singh R 2020 *Nature Photonics* **14** 446–451
[4] O'Brien JL, Furusawa A and Vučković J 2009 *Nature Photonics* **3** 687–695
[5] Wang J, Sciarrino F, Laing A, and Thompson M 2020 *Nature Photonics* **14** 273–284
[6] Yesilkoy F, Arvelo ER, Jahani Y, Liu M, Tittl A, Cevher V, Kivshar Y and Altug H 2017 *Nature Photonics* **13** 390–396
[7] Lee Y, Kim SJ and Lee B 2017 *Sensors* **17** 1726
[8] Pierangeli D, Marcucci G and Conti C 2019 *Phys. Rev. Lett.* 122, 213902
[9] Lemoult F, Kaina N, Fink M and Lerosey J 2013 *Nature Physics* **9** 55–60
[10] Pendry JB,Schurig D and Smith DR 2006 *Science* **312** 5781 1780-1782
[11] Kadic M, Milton GW, van Hecke M and Wegener M 2019 *Nature Reviews Physics* **1**198–210
[12] Cai W and Shalaev V 2009 *Optical metamaterials: fundamentals and applications* Springer, New York.
[13] Zhao Q, Zhou J, Zhang F and Lippens D 2009 *Mater. Today* **12** 60–69
[14] Jahani S and Jacob Z 2016 *Nat. Nanotech.* **11** 23–36
[15] Staude I and Schilling J 2017 *Nature Photonics* **11** 274-284
[16] Kildishev A V, Boltasseva A and Shalaev V 2013 Science 339 6125
[17] Yu N and Capasso F 2014 *Nature Materials* **13** 139-150
[18] Yu N, Genevet P, Kats MA, Aieta F, Tetienne JP, Capasso F and Gaburro Z 2011 *Science* **334**, 333-337
[19] Zhao Y and Alu A 2011 *Phys. Rev*. B **84** 205428
[20] Haoran R et al. 2019 *Nature Communications* 10 2986
[21] Hsiao H H, Chu CH and Tsai DP 2017 *Small Methods* 1600064-1600084
[22] Joannopoulos JD, Johnson SG, Winn JN and Meade R 2008 *Photonic Crystals. Molding the flow of lig*ht -2nd edition Princeton University Press, Oxfordshire OX20 1SY
[23] Kim S, Song H, Ahn H, Won Jun S, Kim S, Min Song Y, Yun Yang S, Kim CS and Kim K 2020 *Nanophotonics*, **9**(9), 2847-2859
[24] Quan LN, Kang J, Ning CZ and Yang P 2019 Chem. Rev. 119 15 9153–9169
[25] Dalacu D, Mnaymneh K, Lapointe J, Wu X, Poole PJ, Bulgarini G, Zwiller V and Reimer EM 2012 *Nano Lett*. **12** 11 5919–5923
[26] Kim H, Lee W, Farrel A C, Morales JSD, Senanayake P, Prikhodko SV, Ochalski TJ and Huffaker D 2017 *Nano Lett.* **17**, 6 3465–3470
[27] Quan LN, Kang J, Ning CZ, and Yang P 2019 *Chem. Rev.* **119** (15) 9153–9169
[28] Anttu N, Abrand A, Asoli D, Heurlin M, Åberg I, Samuelson L, and Borgström M 2014 *Nano Research* **7**(6) 816–823
[29] Fountaine KT, Cheng WH, Bukowsky CR, and Atwater HA 2016 *ACS Photonics* **3** 1826–1832
[30] Madaria AR, Yao M, Chi C, Huang N, Lin C, Li R, Povinelli ML, Dapkus PD, Zhou C 2012 *Nano Lett.* **12**(6) 2839–2845
[31] Wallentin J, *et al* 2013 *Science* **339**(6123) 1050-1060
[32] Garnett E, Yang P 2010 *Nano Lett.* **10** 1082–1087
[33] Kim H, Lee W, Farrell AC, Morales JSD, Senanayake P, Prikhodko SV, Ochalski TJ, Huffaker DL 2017 *Nano Lett.* **17** (6) 3465–3470
[34] Karimi M, Zeng X, Bernd Witzigmann B, Samuelson L, Borgström MT, and Pettersson H 2019 *Nano Lett.* **19** 8424−8430
[35] Chen Y, Kivisaari P, Pistol ME, and Anttu N 2016 *Nanotechology* **27** 435404
[36] Anttu N, and Xu HQ 2013 *Opt. Express* **21**(S3) A558-A575
[37] Floris F, Fornasari L, Bellani V, Marini A, Banfi F, Marabelli F, Beltram F, Ercolani D, Battiato S, Sorba L and Rossella F 2019 *Materials* **12** (21) 3572
[38] Hobbes RG, Petkov N and Holmes JD 2012 *Chem. Mater.* **24** 11 1975-1991
[39] Li Q and Lau KM 2017 *Progress in Crystal Growth and Characterization of Materials* **63** 4 105-120
[40] McIntyre P C, Fontcuberta i Morral A 2020 *Materials Today Nano* **9** 100058
[41] Güniat L, Caroff P and Fontcuberta i Morral A 2019 *Chemical. Reviews* **119** (15), 8958-8971
[42] Wagner RS. and Ellis WC. 1964 *Applied physics letters* **4**, 5, 89 90
[43] Mårtensson T, Borgstrom M, Seifert W, Ohlsson B J and Samuelson L 2003 *Nanotechnology* **14** 1255–1258
[44] Dalacu D, Kam A, Austing D G, Wu X, Lapointe J, Aers G C and Poole P J 2009 *Nanotechnology* 20 395602
[45] Otnes G, Heurlin M, Graczyk M, Wallentin J, Jacobsson D, Berg A, Maximov I and Borgström M T 2016 *Nano Research* **9**(10) 2852–2861
[46] Garnett E, Mai L, and Yang P 2019 *Chemical Reviews* 119 15 8955-8957

[47] Tomioka K, Ikejiri K, Tanaka T, Motohisa J, Hara S, Hiruma K and Fukui T 2011 *J. Mater. Res.* **26** 2127–41
[48] Vukajlovic-Plestina J et al. 2019 *Nat Commun* **10** 869
[49] Messing ME, Hillerich K, Johansson J, Deppert K, Dick K A 2009 *Gold Bulletin* **42** 3
[50] Caroff P, Messing M E, Borg M B, Dick K A, Deppert K and Wernersson LE 2009 *Nanotechnology* **20** 495606
[51] Otnes G and Borgström MT 2017 *Nanotoday* **12** 31-45
[52] Sadre-Momtaz Z, Servino S, Demontis V, Zannier V, Ercolani D, Rossi F, Rossella F, Sorba L, Beltram F and Roddaro S 2020 *Nano Lett.* **22** 1693-1699
[53] Prete D, Erdman PA, Demontis V, Zannier V, Ercolani D, Sorba L, Beltram F, Rossella F, Taddei F and Roddaro S 2019 *Nano Lett.* **19** 5 3033–3039
[54] Cornia S, Rossella F, Demontis V, Zannier V, Beltram F, Sorba L, Affronte M, Ghirri A 2019 Scientific Reports 9 19523
[55] Rocci M, Rossella F, Gomes UP, Zannier V, Rossi F, Ercolani D, Sorba L, Beltram F, Roddaro S 2016 *Nano Lett.* **16** 7950-7955
[56] Ji X, Yang X, Du W, Pan H, Luo S, Ji H, Xu H Q, Yang T 2016, *Nanotechnology* **27** (27), 275601
[57] Gibson SJ, van Kasteren B, Tekcan B, Cui Y, van Dam D, Haverkort JEM, BAkkers EPAM and Reimer ME 2019 *Nat. Nanotechnol.* **14** 473–479
[58] Demontis V, Marini A, Floris F, Sorba L and Rossella F 2020 *AIP Conference Proceedings* **2257** 020009
[59] Zhang G, Sasaki Satoshi, Tateno K, Gotoh H and Sogawa T 2013 *AIP Advances* **3**, 052107
[60] Lumerical Inc. Available online: http://www.lumerical.com/tcad-products/fdtd/
[61] Floris F et al. 2017 *Nanomaterials* **7**, 400
[62] Jensen LE, Björk MT, Jeppesen S, Persson, Ohlsson BJ, Samuelson L 2004 *Nano Lett.* **4**, 1961
[63] Floris F, *et al* 2014 *J. Phys. Chem. Lett.* **5**(17) 2935–2940